Energy Conversion and Management 204 (2020) 112218

Contents lists available at ScienceDirect

Energy Conversion and Management

journal homepage: www.elsevier.com/locate/enconman

Numerical and experimental investigation of a compound parabolic concentrator-capillary tube solar collector

Rong Ji Xu[a,*], Yuan Qiang Zhao[a], Hao Chen[a], Qing Ping Wu[b], Li Wei Yang[c], Hua Sheng Wang[c]

[a] Beijing Engineering Research Center of Sustainable Energy and Buildings, Beijing University of Civil Engineering and Architecture, Beijing 100044, China
[b] School of Energy and Power Engineering, Xi'an Jiaotong University, Xi'an 710049, China
[c] School of Engineering and Materials Science, Queen Mary University of London, London E1 4NS, UK

ARTICLE INFO

Keywords:
Solar energy
Compound parabolic concentrator
Solar collector
Capillary tube
Numerical simulation

ABSTRACT

The paper reports numerical and experimental investigation of a compound parabolic concentrator-capillary tube solar collector (CPC-CSC). The capillary tube having an outer diameter 4 mm is used as the absorber, which reduces the size of the solar collector and achieves a concentration ratio of 4.22 in comparison with the same thickness 75 mm of a flat-plate solar collector. The horizontal CPCs separate the air layer into smaller cells, resulting in decrease in heat loss through the air layer. Details of the design and work principle of the new collector are described. Both experimental and numerical studies were carried out for the purpose of operating characteristics and thermal performance of the solar collector. The effect of solar irradiation intensity and inlet water temperature were tested based on the standard of GB/T 4271-2007. A three-dimensional model of the collector is developed and its performance is numerically simulated using FLUENT. The influence of solar irradiation intensity, velocity of ambient air, glass thickness, insulation thickness, inclination angle, mass flow rate and inlet temperature of water are analyzed. The results of numerical were verified by experimental data and the maximum deviation is found to be 15%. The numerical results suggest that: 1) the main heat losses of the CPC-CSC is due to the heat leakage through the air layer between glass cover and CPC; 2) the collector efficiency decreases as the convective heat transfer of the air layer increases; 3) when the solar irradiation intensity rises, the surface temperature of collector tubes increases, enhancing air layer convection and thus reducing collector efficiency; 4) with the increase in mass flow rate of water in the pipe, the heat absorption of water in the pipe increases and thus the collector efficiency increases and 5) the velocity of ambient air, glass thickness, insulation thickness, and inclination angle have little effects on the performance of the solar collector.

1. Introduction

Solar energy is one of the richest and cheapest clean energies which can satisfy increasing global energy demands. Solar hot water system is an efficient way to make use of solar energy [1]. Flat-plate solar collectors are the most commonly used type of low-to-medium temperature solar collectors [2]. Their thermal performance is limited mainly by the low absorption rate of solar energy and high heat loss to surroundings. The major heat loss occurs by convective heat transfer through the air layer inside the collector. So far, many studies have been attempted to improve their efficiency. Zhu et al. [3] proposed a new type of solar air collector using flat micro-heat pipe arrays (FMHPA) and evacuated tubes. Their results show that the thermal efficiency of the collector reaches 73% under stable operation in summer. Kundu [4] found that the thermal performance of the solar collector increases with the increase in ambient temperature. Aerogel [5] and solar reflector [6] were used to improve the thermal efficiency of flat-plate collectors. The results show that aerogel can greatly improve the thermal efficiency, 1.66 times higher than the ordinary ones without using aerogel. The reflector improves the thermal efficiency around 10%. Beikircher et al. [7] presented advanced insulation methods. The heat loss from the front of the collector was reduced by transparent insulation materials while the heat loss from the rear was reduced by an integrated vacuum super insulation (VSI). At a reduced temperature difference of 0.1 $K \cdot m^2/W$, the collector could achieve a thermal efficiency higher than 50%. He et al. [8] studied the effect of Cu-H_2O nanofluids and their thermal conductivity on the thermal efficiency. The experimental results show that the use of Cu-H_2O nanofluids as the absorption working fluid increases the thermal efficiency by 23.8%. Ahmadi et al. [9] studied the effect of graphene nanofluids

* Corresponding author.
E-mail address: xurongji@bucea.edu.cn (R.J. Xu).

https://doi.org/10.1016/j.enconman.2019.112218
Received 12 August 2019; Received in revised form 22 October 2019; Accepted 23 October 2019
Available online 20 December 2019
0196-8904/

Nomenclature

A	area of collector, $L \times W$ (1200 × 640)
CR	concentration ratio of CPC
d	diameter
d_{in}	inner diameter
d_{out}	outer diameter
D	aperture width
H	height
I	solar irradiation intensity
L	length
Q	heat
Q_w	heat absorbed by water
T_{in}	inlet temperature of water
T_{out}	outlet temperature of water
W	width

Greek symbols

η	efficiency of solar collector
β_a	thermal expansion coefficient of air
ρ_{amb}	air density at qualitative temperature
ρ_a	air density at ambient temperature
φ	angle between the incident ray and the x-axis
θ_A	aperture angle of CPC

on the thermal performance. The results indicate that dispersing grapheme in the base fluid can increase thermal efficiency up to 18.9%.

The compound parabolic concentrator (CPC) is a non-imaging component with low focusing degree, which is designed based on edge optics [10]. It can make sunlight reach the receiving surface after multiple reflections within a given receiving angle. The CPC solar collector has a simple structure and operates readily since it does not require real-time position tracking of the sun [11]. Its working temperature can reach the range of 80 °C–250 °C, suggesting that it can be used to realize the medium-temperature application of solar energy [12]. Such an effective collection of solar energy enables almost the theoretical thermal efficiency and therefore demonstrates a promising prospect of these collectors in the low-to-medium temperature applications.

Many investigations of CPC solar collectors have been performed. Zheng et al. [13] presented a combination of a CPC solar collector and a flat plate solar collector. Its thermal efficiency can achieve up to 60.5%. Xu et al. [14] reported an experimental investigation of a novel solar collector that integrated a CPC and a closed-end pulsating heat pipe (PHP). The results show that its instantaneous thermal efficiency can reach up to 50% when the direct normal solar irradiation intensity is 800 W/m^2. Gu et al. [15] demonstrated a new solar thermal collector which can obtain very high temperature up to 600 °C, providing heat in small size for various portable applications. Pradhan et al. [16] investigated the thermal performance of a solar collector integrated CPC and heat pipe embedded evacuated tube for medium-temperature applications. The experimental results show that the collector can provide sufficiently high temperature for water boiling application. Al-Imam et al. [17] examined a hybrid photovoltaic/thermal collector using phase change material (PCM) to store thermal energy. Its thermal efficiency varies from 40% to 50% for clear day and around 40% for semi-cloudy day. Khalifa et al. [18] presented a structure employing two tubulous collectors in a CPC collector, which can improve the optical efficiency and thermal performance. Zou et al. [19] reported a solar collector using small parabolic groove, which can operate for low-temperature fluid and perform good anti-frosting under cold climate conditions. When the solar irradiation intensity is less than 310 W/m^2, its thermal performance can reach about 67%. Chamasa-Ard et al. [20] designed a solar collector with evacuated tube and CPC with the measured thermal performance 78%, based on the standard of ISO 9806-1. Oommen et al. [21] designed a solar collector using CPC with thermal efficiency of 50% at high temperature. Tchinda [22] developed a mathematical model for CPC air heater to evaluate the thermal performance of the solar collector. The effects of key parameters on thermal performance such as the collector length, mass flow rate of air and wind speed were presented. Abdullahi et al. [23] founded that the thermal performance of the tracking CPC solar collector was better than the same solar collector without tracking.

In this work, a solar collector integrating CPC and capillary tubes is proposed. A model is developed and the thermal performance of the solar collector is numerically simulated to investigate the effects of main parameters. A prototype of the solar collector is designed and built and its thermal performance is tested under different working conditions. The numerical simulation results are compared with measured data. The operating characteristics and thermal performance of the new collectors under different working conditions and structures are studied. It introduced an efficient way to achieve low-to-medium temperature solar heat collecting.

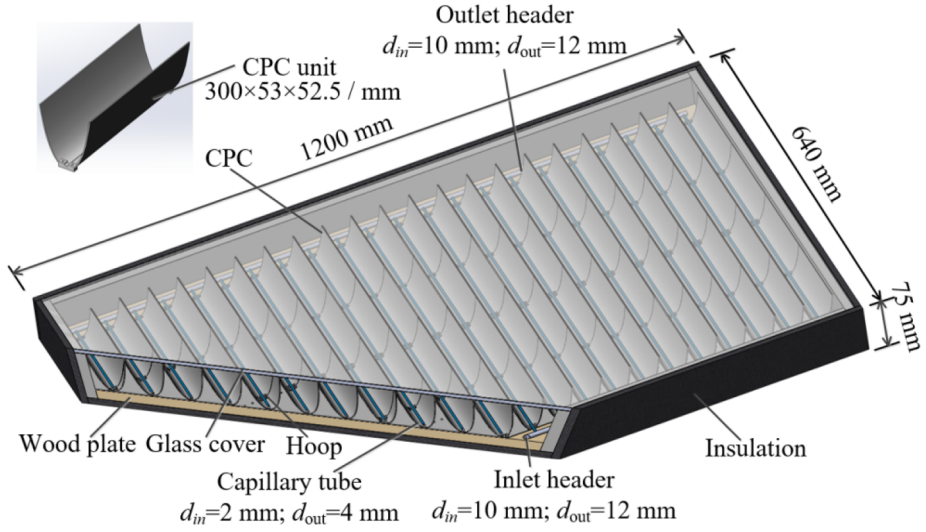

Fig. 1. Schematic of the CPC-CSC.

Table 1
Dimensions of solar collector, CPC, header and capillary tube.

Dimension	Value
Dimension of solar collector, mm	$L = 1200$, $W = 640$, $H = 70$
Dimension of a CPC unit, mm	$L = 300$, $W = 53$, $H = 52.5$
Diameter of inlet and outlet headers, mm	$d_{in} = 10$, $d_{out} = 12$
Diameter of capillary tube, mm	$d_{in} = 2$, $d_{out} = 4$

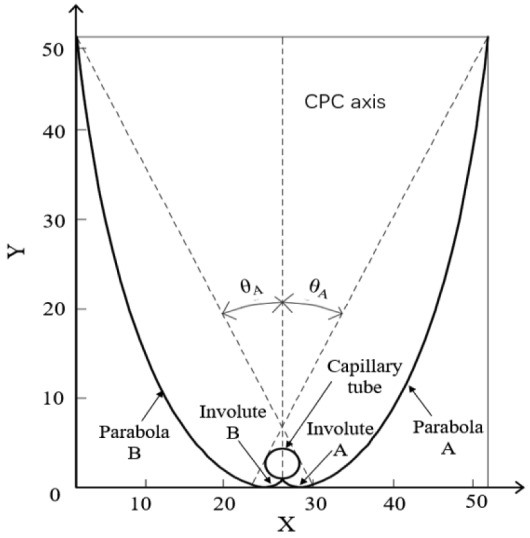

Fig. 2. Geometry and dimension of CPC, capillary tube absorber and co-ordinator.

2. Experimental system

2.1. The new solar collector

The new solar collector adopts CPC as concentrators and capillary tubes as absorbers placed at the involute circle of CPC (named as CPC-CSC), as shown in Fig. 1. The CPCs concentrate solar irradiation onto the capillary tubes, heating the working fluid flowing in the capillary tubes. It has a total length of 1200 mm, a thickness of 75 mm, a width of 640 mm and an effective heat collecting area of 0.699 m^2. The collector consists of a glass cover, CPC, capillary tube absorber, insulation, and baseplate. The glass cover is a single-layer high-transparent glass with a thickness of 5 mm. The absorber is composed of 22 parallel copper capillary tubes, each of which has an outer diameter of 4 mm, an inner diameter of 2 mm and a length of 610 mm. Two copper tubes with an outer diameter of 12 mm and an inner diameter of 10 mm serve as inlet and outlet headers to connect the capillary tubes forming the flow paths. The dimensions of the collector are given in Table 1. To prevent heat loss through the envelope, the four sides and baseplate are insulated. Water is used as the working fluid.

Fig. 1 shows the layout of the collector. 44 CPC units are arranged in 22 columns and each column has two CPC units. The CPC units, made by additive manufacturing, have a groove depth of 52.5 mm, a length of 300 mm and an opening width of 53 mm. The reflector surface is coated by a layer of reflective aluminum foil with a thickness of 0.1 mm and a reflectivity of 0.85. The concentration ratio is 4.22. The capillary tubes are fixed at the two ends of CPCs using buckles and then fixed on the baseplate.

2.2. The CPC

The CPC, a non-imaging low-focusing concentrator, is designed based on the principle of edge optics, to collect incident sunlight onto the receiver in a given range of acceptance angles for an ideal concentrating ratio. The CPC is composed of two pairs of symmetrical curves (see Fig. 2). The curve is given by Eqs (1) and (2) [24].

$$\begin{cases} X = \frac{d}{2}(\sin\varphi - \varphi\cos\varphi) \\ Y = -\frac{d}{2}(\varphi\sin\varphi + \cos\varphi) \end{cases} (0 \le \varphi \le 90^\circ + \theta_A) \quad (1)$$

$$\begin{cases} X = \frac{d}{2}(\sin\varphi - A^*\cos\varphi) \\ Y = -\frac{d}{2}(A^*\sin\varphi + \cos\varphi) \end{cases} (90^\circ + \theta_A \le \varphi \le 270^\circ - \theta_A) \quad (2)$$

where

$$A^* = \frac{\frac{\pi}{2} + \theta_A + \varphi - \cos(\varphi - \theta_A)}{1 + \sin(\varphi - \theta_A)} \quad (3)$$

$$\theta_A = \arcsin\left(\frac{1}{CR}\right) \quad (4)$$

$$CR = \frac{D}{\pi \times d} \quad (5)$$

and φ is the angle between the incident ray and the X-axis.

2.3. The working principle of the CPC-CSC

The solar collector transfers concentrated solar irradiation into thermal energy and the mechanism is illustrated in Fig. 3. The solar irradiation reaching the glass cover is divided into reflected, absorbed and transmitted proportions. The transmitted solar irradiation reaches the CPC inner surface and is concentrated on the surface of capillary tubes, most of which is absorbed by the working fluid. A small proportion of the heat is lost to surroundings by conduction, convection and radiation heat transfer.

The transient heat collecting efficiency of the solar collector is defined as the ratio of actual heat absorbed by water Q_W to solar irradiation reached to the collector IA given by Eq. (6).

$$\eta = \frac{Q_W}{IA} \quad (6)$$

Fig. 4 shows the comparison of the CPC-CSC and flat-plate

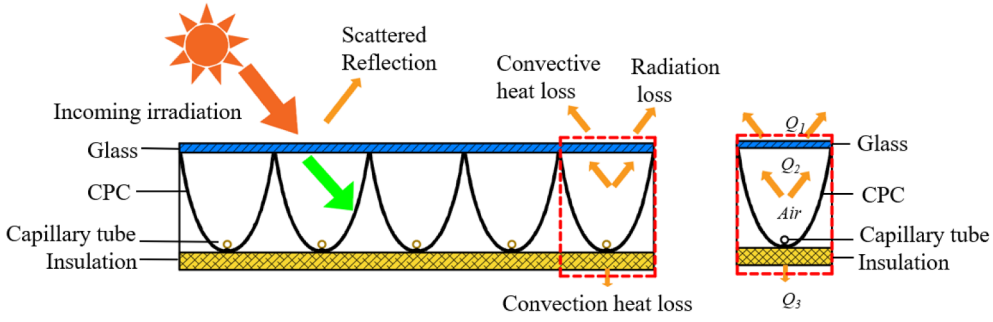

Fig. 3. Mechanism of energy transfer in solar collector.

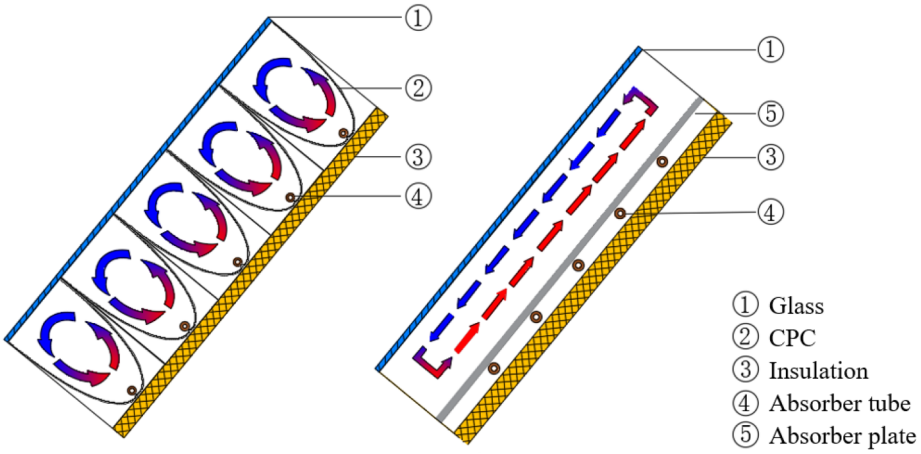

Fig. 4. Comparison of air layers for CPC-CSC and flat-plate solar collector.

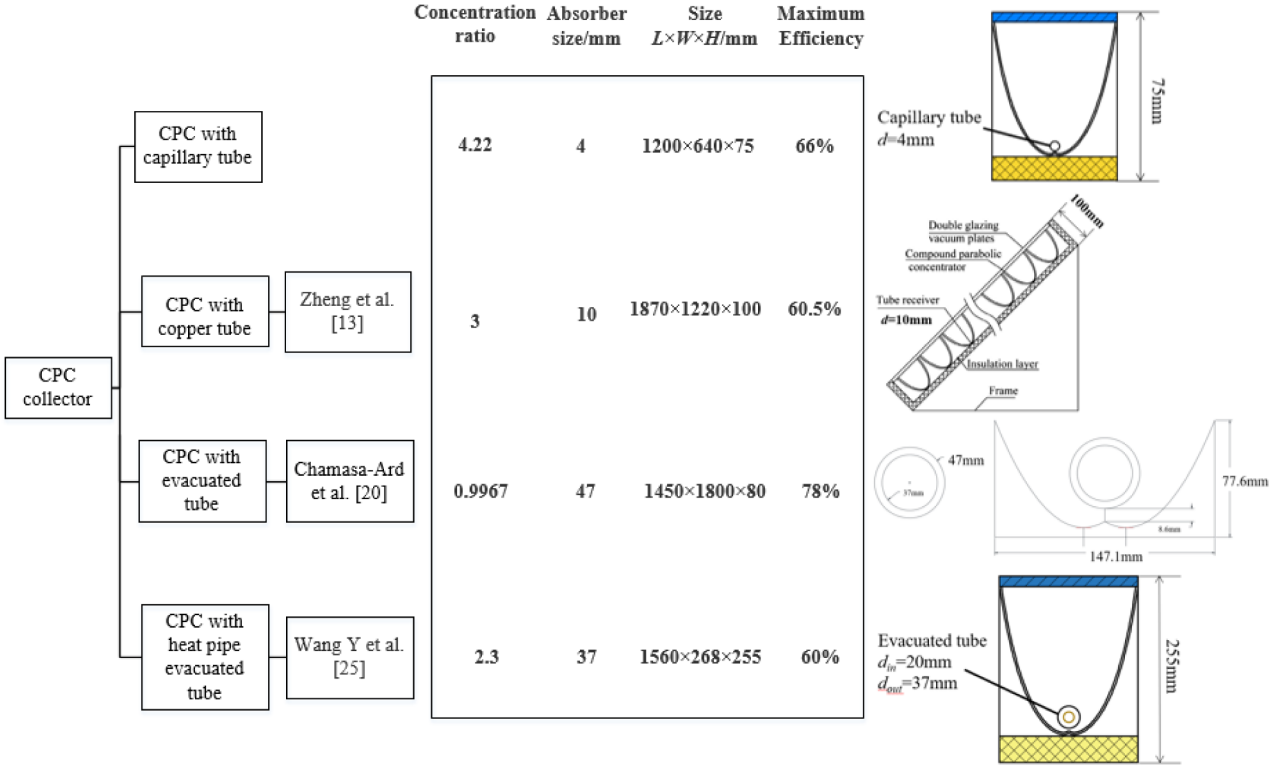

Fig. 5. Comparison of the present CPC-CSC and other types of CPC solar collectors.

collectors. It is seen that the new collector can achieve a higher collection temperature and efficiency due to two advantages: 1) The utilization of capillary tubes reduces the area of heat transfer surface and hence the heat loss by radiation and convection from a higher-temperature surface; 2) Horizontal CPCs separate the air layer into small cells and decrease convective heat transfer.

Copper tubes and evacuated tubes are widely used as the absorbers of CPC collectors. The CPC-CSC in this work is thinner compared with other CPC solar collectors shown in Fig. 5, allowing easy integration with building in practical applications.

The disadvantages of the usage of capillaries are deformation and high flow resistance. Deformation is the biggest problem of capillaries, especially copper tubes. However, deformation merely has influence on brass tubes and stainless-steel tubes. Since the capillaries are multi-parallel, the actual flow area is larger than that of the main tube. In the present study, the flow resistance is not significant.

2.4. Experiment setup

To measure the thermal performance of the CPC-CSC, an experimental setup was built on the roof of a building in Beijing (N 39 °48′, E 116 °28′). Fig. 6 shows the schematic of the setup and Fig. 7 shows its photographs. It consists of CPC-CSC, hot water circulation loop and data acquisition system. The CPC-CSC, assembled as discussed in section 2.1, was put on an adjustable angle bracket in the east-west direction. The hot water circulation loop consists of a thermostatic water bath, chiller, pump and turbine flow meter. Water entering the inlet header is uniformly distributed into the parallel capillary tubes and flows into the outlet header. Two mixers are located at the inlet and outlet of the headers, allowing sufficient mixing of the flow and accurate measurements of the inlet and outlet bulk temperatures of the working fluid. Two T-type thermocouples with an accuracy of ± 0.1 K are inserted in the two mixers to measure the inlet and outlet bulk

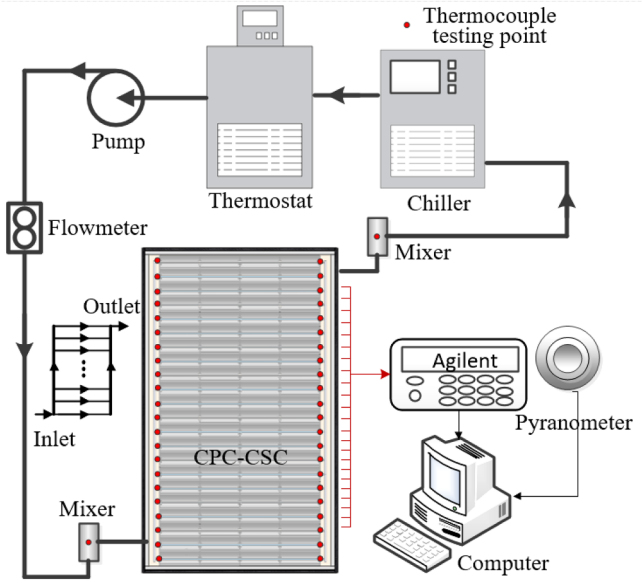

Fig. 6. Schematic of the test rig.

temperatures, respectively. 44 thermocouples are arranged at the inlet and outlet of each capillary tube. The turbine flow meter with an accuracy of 1% measures the mass flow rate of water. The thermostatic water bath is used to provide a constant inlet temperature of water for the solar collector. The solar irradiation intensity is measured by TES-1333R solar radiation recorder (with an accuracy of ± 10 W/m^2). The data acquisition system (Agilent34980A) is used to record temperatures, mass flow rate and solar irradiation intensity. The measurements are conducted in wide ranges of working conditions (see Table 5) according to GB/T 4271-2007.

2.5. Uncertainty analysis

The uncertainties of the measurements includes turbine flow meter (with an accuracy of 1%), T-type thermocouple (with an accuracy of ± 0.1 K), TES-1333R solar radiation recorder (with an accuracy of ± 10 W/m^2). The uncertainty of the thermal efficiency of the solar collector can be calculated using Eqs. (6) and (7) [14].

$$w_R = \sqrt{\sum \left(\frac{\partial R}{\partial x_i} w_i\right)^2} \tag{7}$$

where w_R is the uncertainty of the dependent variable and w_i are the uncertainties of the independent variables. Table 2 summarizes the uncertainty of the quantities.

Table 2
Uncertainties of quantities.

Quantity	Uncertainty
T type thermocouple, K	± 0.1
Turbine flow meter	2.50%
TES-1333R solar radiation recorder, W/m^2	± 10
Thermal efficiency	10.4%

3. Numerical simulation of the computational domain

Ansys-Fluent is used to numerically simulate the thermal performance of the new solar collector based on a three-dimensional model.

3.1. Physical model

A typical unit of the 22 parallel units is chosen as the computational domain, and the modeling ratio is 1:1 (see Fig. 8). The actual dimensions of the domain are the length L_D = 600 mm, width W_D = 53 mm, height H_D = 75 mm and an irradiated area of 0.0318 m^2.

The collector is located in open wind environment. The two ends of the domain are assumed adiabatic. The two side surfaces of the domain are symmetrical boundary conditions. The upper surface of the collector involves convective and radiation heat transfer and the bottom surface of the baseplate involves convective heat transfer. The dimensions of the materials and their thermophysical properties are given in Table 3. Pure water is used as the working fluid.

The following assumptions and approximations are made:

(1) The incidence solar radiation is assumed to be perpendicular to collector surface and solar radiation reaching the surface of capillary tubes is completely absorbed.

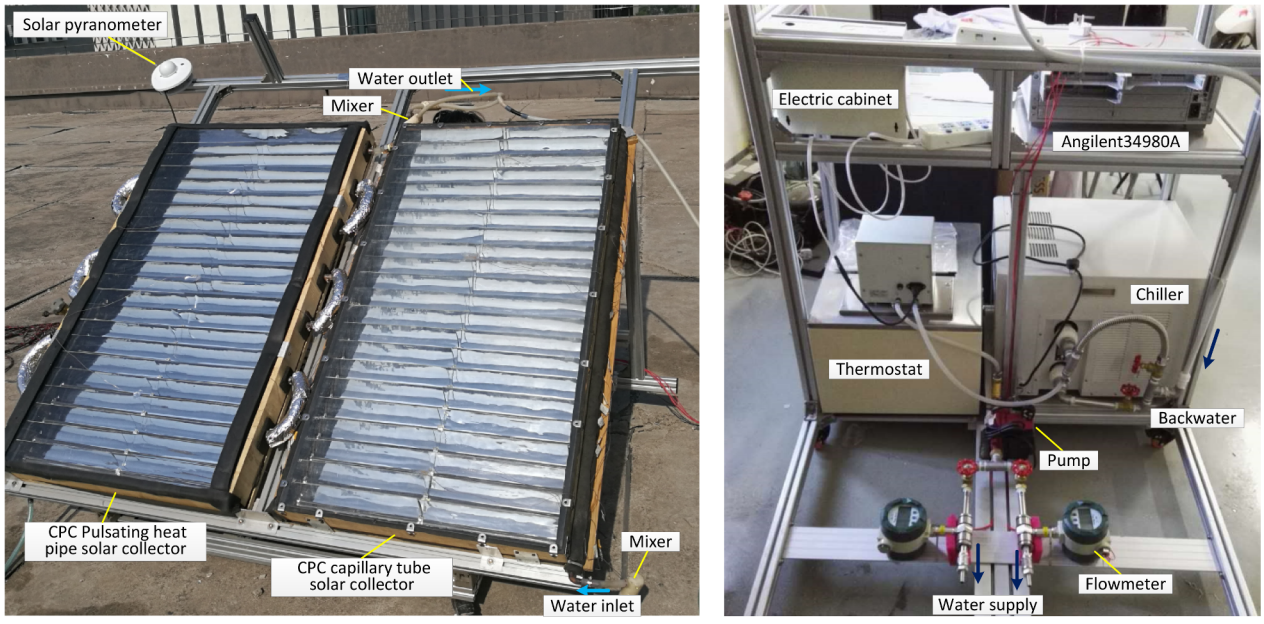

Fig. 7. Photos of the test rig.

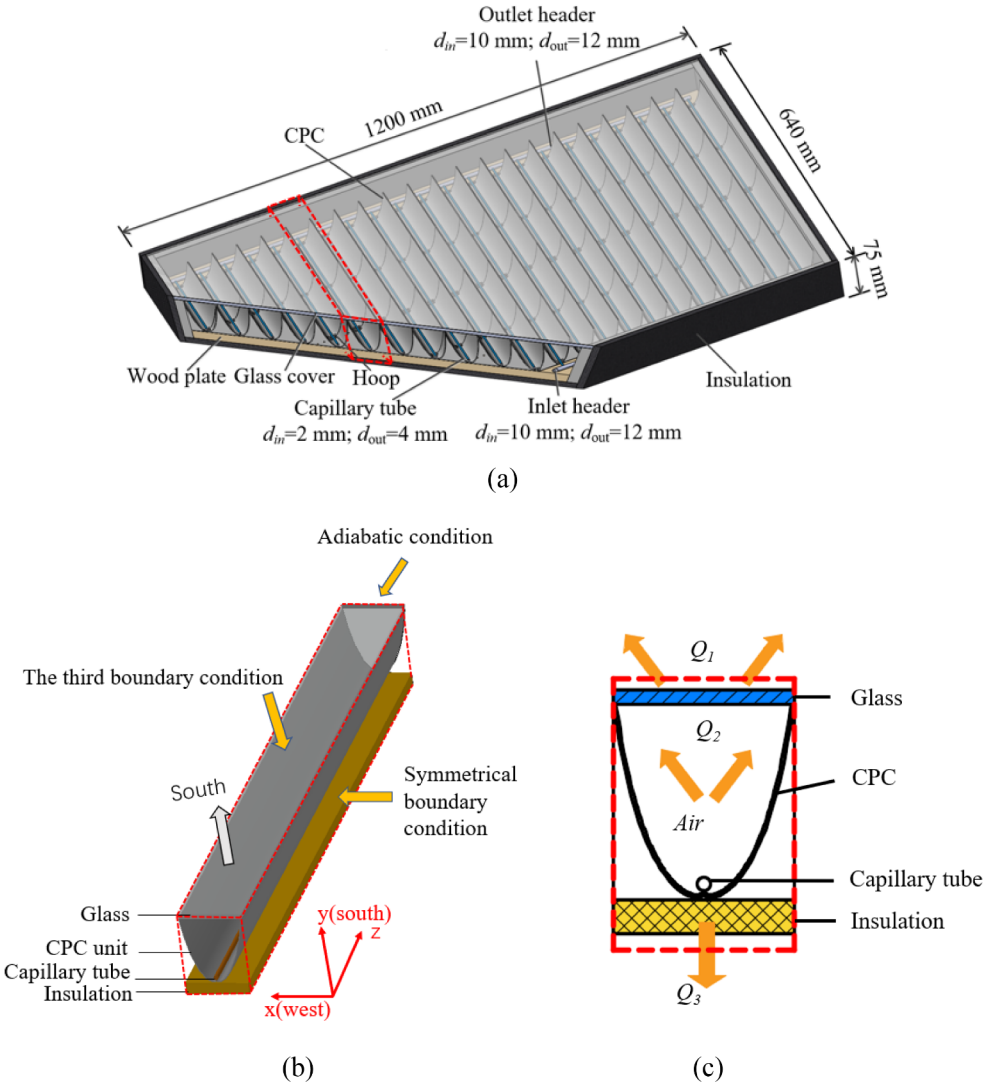

Fig. 8. Computational domain: (a) the domain in the CPC-CSC, (b) details of the domain, (c) cross-sectional view of the domain.

Table 3
Thickness and properties of CPC-CSC materials and air layer.

Material	Thickness mm	Thermal conductivity W/(m K)	Density kg/m^3	Specific heat J/(kg K)
Glass	4	0.76	2500	790
Air	–	0.0267	1.225	1005
CPC material (ABS plastic)	1	0.25	1050	1591
Thermal insulation material	20	0.034	54	1500
Capillary tube material (copper)	1	387.6	8978	381

(2) Air flow inside the collector is natural convection.
(3) The properties of air, water and solid materials are independent of temperature.

3.2. Governing equations

The collection process combines heat conductivity, convection, and radiation heat transfer. Convective heat transfer occurs between the outer wall of the capillary tube and the air layer. The flow inside the collector tube is regarded as a 3D, steady, constant-property, laminar flow. Considering the heat transfer process, governing equations [26] are following:

Conservation of mass:

$$div(U) = 0 \tag{8}$$

Conservation of momentum:

$$div(u\vec{U}) = div(vgradu) - \frac{1}{\rho}\frac{\partial p}{\partial x} \tag{9}$$

$$div(v\vec{U}) = div(vgradv) - \frac{1}{\rho}\frac{\partial p}{\partial y} \tag{10}$$

$$div(w\vec{U}) = div(vgradw) - \frac{1}{\rho}\frac{\partial p}{\partial z} \tag{11}$$

Conservation of energy equation for fluid and solid are respectively:

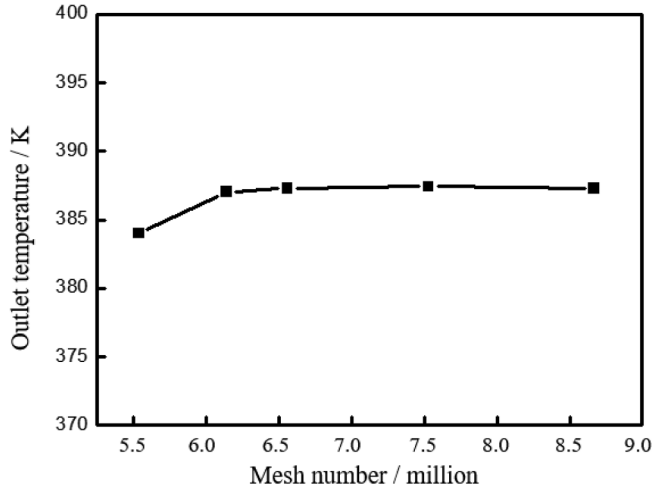

Fig. 9. Verification of mesh independence.

$$div(\vec{U}T) = div\left(\frac{\lambda}{\rho c_p} gradT\right) \tag{12}$$

$$\frac{\partial T^2}{\partial x^2} + \frac{\partial T^2}{\partial y^2} + \frac{\partial T^2}{\partial z^2} = 0 \tag{13}$$

For convection of air inside the collector, the Boussinesq assumption is taken to calculate the density.

$$(\rho_a - \rho_{amb})g = -\rho_{amb}\beta_a(T - T_{amb})g \tag{14}$$

where ρ_a is the air density, ρ_{amb} is density of ambient air at its temperature T_{amb}, and β_a is the thermal expansion coefficient of air.

3.3. Boundary conditions

The boundary conditions of the domain are:

For the domain:

Upper and lower surfaces at *x-z* plane y = 0, H_D: the convection boundary condition with air temperature given;

Front and back end surfaces at *x-y* planes $z = 0$, L_D: adiabatic condition;

Left and right surfaces at *y-z* planes $x = 0$, W_D: symmetrical boundary condition.

For air inside collector:

The non-slip boundary conditions are applied to all solid-air interfaces.

For water flow in capillary tubes:

At the inlet: velocities $u = u_{in}$, $v = 0$, $w = 0$; temperature $T = T_{in}$;

At the outlet: partial unidirectional condition;

The non-slip boundary condition is applied to the solid-water interface.

Since the diameter of the copper capillary tubes are small compared with the size of CPCs and hence are regarded as a homogeneous body heat source. All the surface temperatures of solid components are obtained from the coupled numerical simulations of air convection inside the collector, water flowing inside the capillary tubes and heat conduction in the solids.

3.4. Verification of mesh independence

Physical modelling, meshing, and regional and boundary condition settings are conducted in GAMBIT. Within the computational domain, a sharp angle exists between CPC left and right surfaces. The thickness of CPC is only 1 mm and both the inner and outer diameters of capillary tubes are relatively small. These make the meshing process difficult because mesh refinement is required for CPC and capillary tube parts.

Table 4
Summary of the working conditions of numerical simulation.

Working conditions	Solar irradiation intensity (W/m^2)	velocity of ambient air (m/s)	Glass thickness (mm)	Insulation thickness (mm)	Inclination angle (°)	Inlet temperature of water (K)	Mass flow rate of water (kg/h)
Reference condition	1000	2	4	10	45	290	0.23
Case I	300, 500, 800, 1000	2	4	10	45	290	0.23
Case II	1000	0, 1, 2, 3, 4	4	10	45	290	0.23
Case III	1000	2	2, 3, 4, 5, 6	10	45	290	0.23
Case IV	1000	2	4	5, 10, 15, 20, 25, 30	45	290	0.23
Case V	1000	2	4	10	0, 30, 45, 60, 90	290	0.23
Case VI	1000	2	4	10	45	280, 290, 300, 320, 340, 360, 380, 400	0.23
Case VII	1000	2	4	10	45	290	0.23, 0.46, 0.69, 0.92, 1.15

Table 5
Environmental conditions of the experiments.

	Solar intensity (W/m^2)	Ambient temperature (K)	Air velocity (m/s)	Date of experiments
Set 1	290–1000	288–291	1–2	10 Oct. 2016–20 Nov. 2016
Set 2	920–1000	289–293	1–2	5 Apr. 2017–10 May 2017

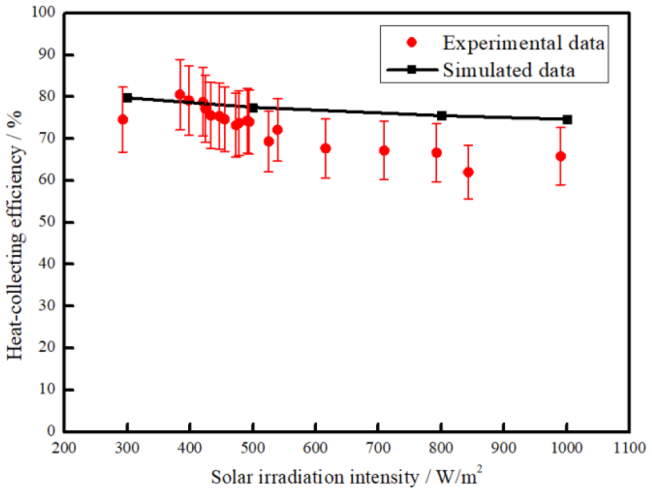

Fig. 10. Comparison of numerical results and experimental data: effect of solar irradiation intensity. Case I.

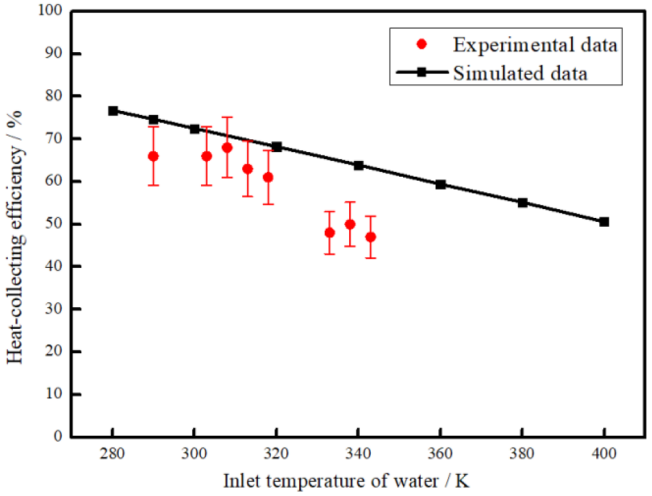

Fig. 11. Comparison of numerical results and experimental data: effect of inlet temperature of water. Case VII.

Therefore, a relatively efficient mesh is built through multi-region partition for the whole simulated domain, then multiple meshing, and adopting different mesh densities in different regions. Several meshing densities have been solved using outlet temperature as determination parameter for mesh independence verification, as shown in Fig. 9. The final determined amount of mesh is around 6.35 million.

3.5. Working conditions of numerical simulation

The numerical simulations are conducted to investigate the influence on the thermal performance of the collector caused by solar irradiation intensity, velocity of ambient air, glass thickness, insulation thickness, inclination angle, mass flow rate and inlet temperature of water. 33 working conditions given in Table 4 are simulated.

3.6. Numerical simulation

The computational domain initialization, residual detector setting, iteration number setting, and calculation are conducted after setting boundary conditions. A surface to surface radiation model is selected to calculate the radiation heat transfer. Finite volume method is employed to disperse governing equations. In terms of the coupling of pressure and velocity, the SIMPLE algorithm is used to disperse flux terms in second-order upwind and diffusion terms in the central differencing scheme. An efficient multi-core CPU workstation (with dual processors of Inter® Xeon® CPU E5-2630 v4 @ 2.20 GHz, a running memory of 64G, and a CPU of 20 cores) is used for parallel computation to improve calculating speed and hence reduce calculating time.

Result statistics are analyzed by FLUENT with post-processing functions. Temperature distribution and heat flux distribution are mainly studied. Statistics investigate the temperature of outlet profile, heat losses and heat absorptions through all side walls, and temperature distribution in each layer. The computational domain is calculated based on the statistics of temperature differences between the inlet and outlet of water. The volume heat of the computational domain should be balanced with the heat absorption of water inside the tubes and heat losses to the surroundings. This can be used to check computational accuracy and calculation convergence.

4. Results and discussion

4.1. Numerical results and comparison with experimental data

The thermal performance of the CPC-CSC is tested based on the standard GB/T 4271-2007. Two sets of experiments as shown in Table 5 were conducted. The first set of experiments examine the effect of solar irradiation intensity (see Case I in Table 4). Fig. 10 shows that the heat collecting efficiency decreases from 75% to 66% as the solar irradiation intensity increases from 290 W/m^2 to 1000 W/m^2. The deviation between the numerical results and experimental data is about 8.5%. This is due to neglecting of the heat losses through four side surfaces of the collector, similar to that in most of the numerical simulations of solar collectors [13,27–28]. The radiations from the capillary tubes to the air layer and from the air layer to the sky are neglected since the absorptivity of air layer is very low. The second set of experiments examine the effect of inlet temperature of water (see Case VII in Table 4). Fig. 11 shows that the heat collecting efficiency decreases from about 67% to 50% as the inlet temperature of water increases from 290 K to 345 K. The deviation between the numerical results and experimental data is within 15%. These good agreements verify the modeling and numerical simulations.

As shown in Fig. 5, CPC was widely used in solar collecting field and copper tubes and evacuated tubes are commonly used as the absorber of CPC collector. A similar structure to present collector but higher thickness was proposed by Zheng et al. [13] and its highest thermal efficency is 60.5%. A tracking CPC solar collector combining CPC and heat pipe evacuated tubular receiver was developed by Wang et al. [25] and its thermal efficency is about 60%. A collector intgrated CPC with evacuated tube was proposed by Chamasa-Ard et al. [20] and its thermal efficency is 78%, which is higher than prsent study.

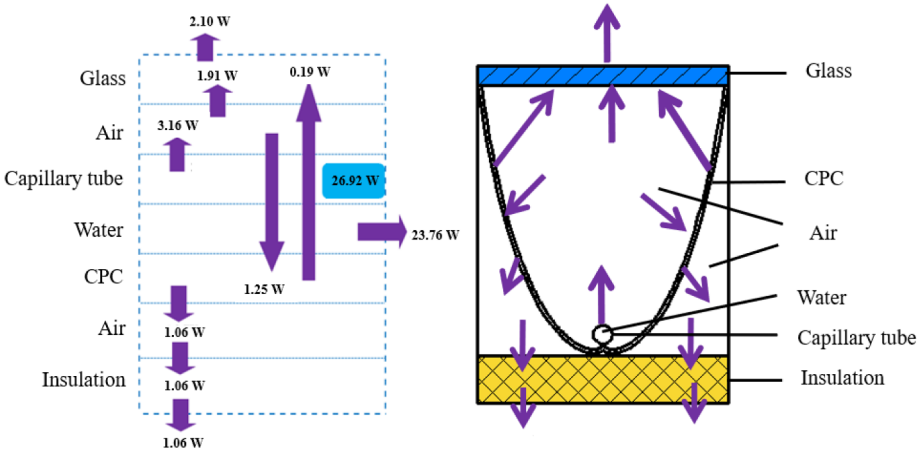

Fig.12. Mechanism of heat transfer in the reference condition: (a) quantitative analysis and (b) schematic.

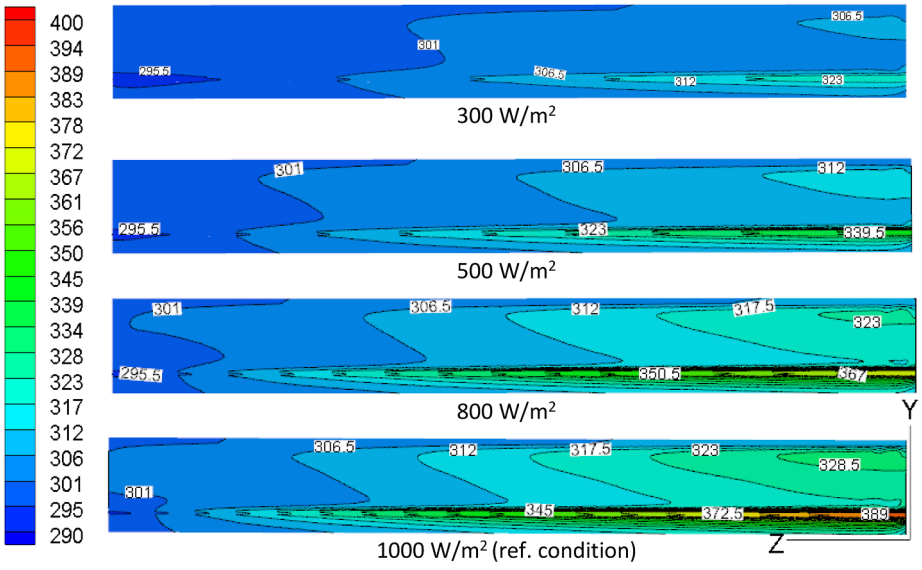

Fig. 13. Temperature profiles at plane $x = 0$ for solar irradiation intensity 300, 500, 800 and 1000 W/m^2.

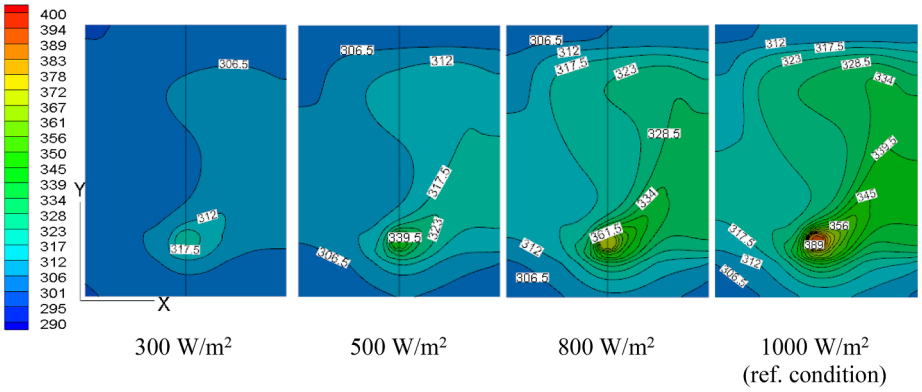

Fig. 14. Temperature profiles at the outlet plane for solar irradiation intensity 300, 500, 800 and 1000 W/m^2.

4.2. Analysis of the collector performance in reference condition

Quantitative statistics and analysis of heat transfer in each layer of the reference condition is performed from the simulation results as illustrated in Fig. 12. The total heat absorbed on the collector tube surfaces is 26.92 W. Heat loss through glass cover is 2.1 W and the heat loss through the insulation baseplate is 1.06 W. Heat absorbed by water flowing inside the tubes is 23.76 W, taking 74.7% of initial heat reaching to the outer surface of the glass cover i.e. 31.8 W.

Analysis based on Fig. 12 shows that the convective heat loss through the air layer between the glass cover and CPC results in the main heat loss of the new solar collector. The CPC can separate the air layer into small cells, suppress large-scale air convection, reduce heat loss and thus improve the solar collector efficiency. The increase in

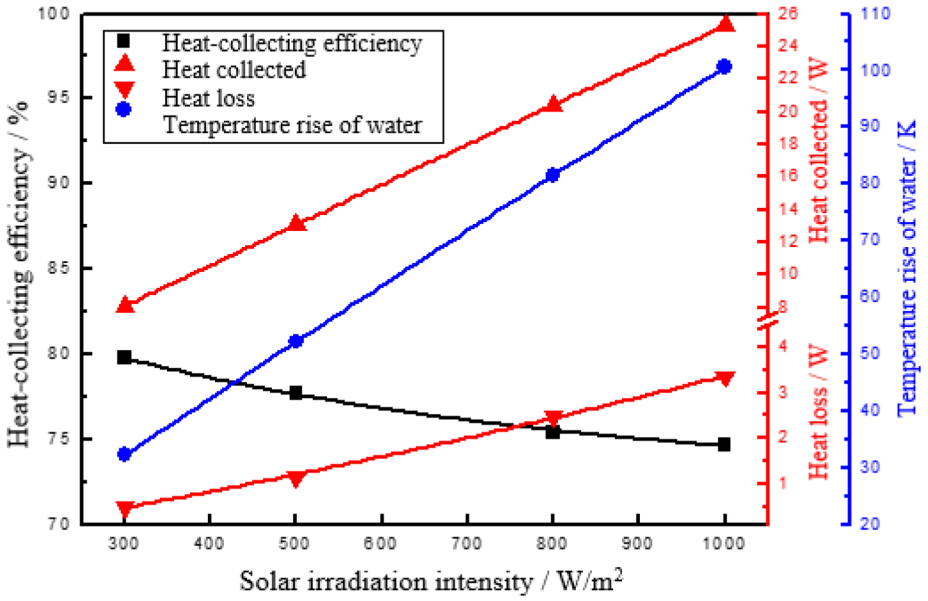

Fig. 15. Effect of solar irradiation intensity on the thermal performance of the CPC-CSC.

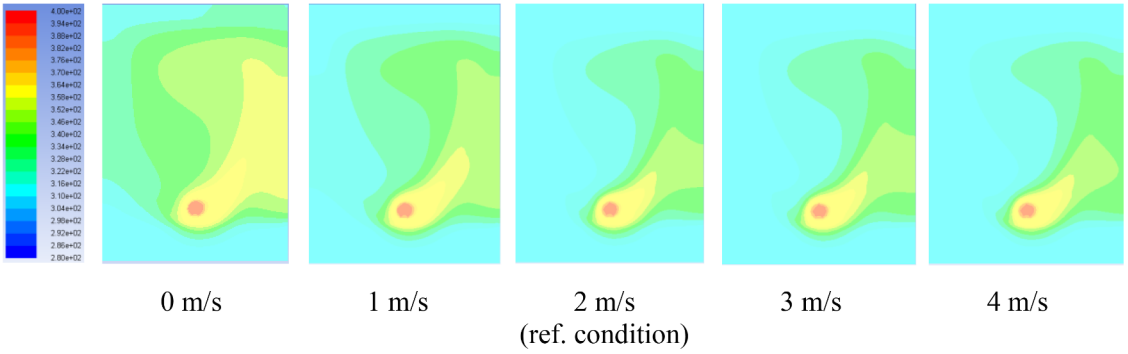

Fig. 16. Temperature profiles at the outlet plane $z = w$ for different velocities of ambient airs.

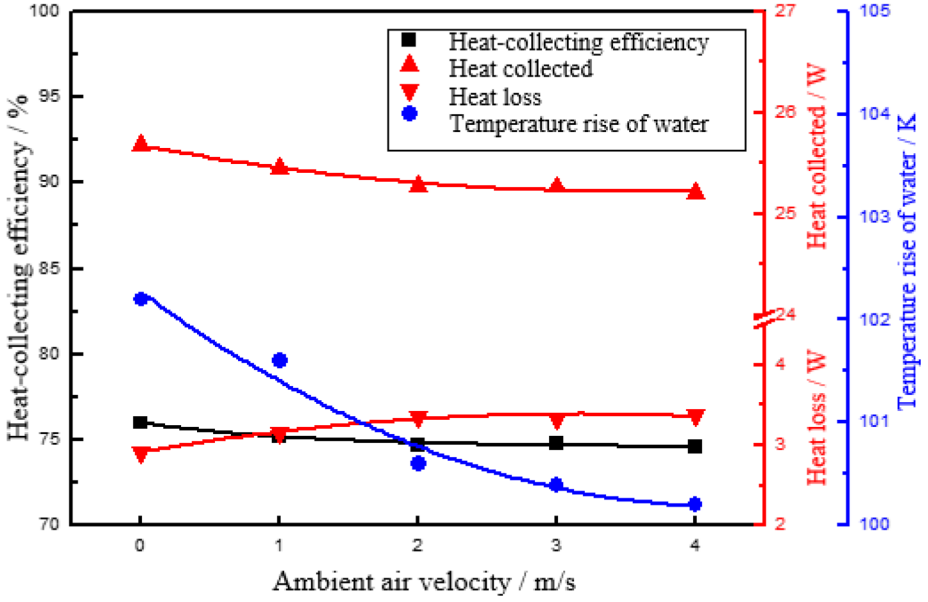

Fig. 17. Effect of ambient air velocity on the thermal performance of the CPC-CSC.

Table 6
Thickness and transmittance of glass cover.

Thickness, mm	2	3	4	5	6
transmittance	91.68%	91.52%	91.36%	91.20%	91.04%

surface temperature of the collector tube enhances the convective heat transfer in the air layer. For a single capillary tube absorber unit, if the temperature rise of water between the inlet and outlet is large, the surface temperature of the collector tube near the outlet is relatively higher. This lead to relatively strong convection in air layer resulting in larger heat loss through the air layer.

4.3. Effect of solar irradiation intensity

Simulations are performed of the computational domain for solar irradiation intensities of 300 W/m^2, 500 W/m^2, 800 W/m^2 and 1000 W/m^2 respectively, and all the other conditions being kept the same as those under the reference condition (see Table 4). Fig. 13 shows the temperature profiles at the plane $x = 0$ for four solar irradiation intensities. As the solar irradiation intensity increases, the outlet temperature of water increases and the temperature gradient of the air side outside the collector tube appears a significant increase. Both the water temperature inside the collector tubes and the temperature of the air layer increase along the direction of water flow. It is seen that the higher collector tube temperature leads to stronger convection in the air layer. Fig. 14 introduces the temperature profiles at the plane $z = w$ for four solar irradiation intensities. When the solar irradiation intensity is 1000 W/m^2, the outlet temperature of water reaches 398 K.

Figure 15 shows the variations of the heat collected, heat loss, temperature rise of water and heat-collecting efficiency with the solar irradiation intensity. It is seen from Fig. 15 that as the solar irradiation intensity increase, the heat absorbed by water inside capillary tubes and the heat losses through the glass cover and insulation baseplate increase. When the solar irradiation intensity increases from 300 to 1000 W/m^2, the heat absorbed by water increases from about 10 W to 25 W. The heat loss increases from about 0.5 W to 3.5 W. When solar irradiation intensity is 300 W/m^2, collector efficiency is 79.8%. While a collector efficiency of 74.7% corresponds to solar radiation intensity of 1000 W/m^2. The thermal performance of the collector has fallen by 5.1%. With the increase in the outer surface temperature of capillary tubes for higher solar irradiation intensity, the convection in the air layer is enhanced and the heat leakage through the glass cover increases.

4.4. Effect of ambient air velocity

The velocity of ambient air can influence the heat loss and efficiency of the solar collector by varying the convective heat transfer between the glass cover and baseplate with the surroundings, and therefore affect collector efficiency. Fig. 16 shows the simulations results of temperature profiles at the outlet plane for four ambient air velocities of 0, 1, 2, 3 and 4 m/s, respectively. The air temperature in computational domain is relatively high and evenly distributed for ambient air velocity 0 (see Fig. 16 (a)) while the temperature distributions of air are similar in other conditions (see Fig. 16 (b)–(d)). Fig. 17 displays the variations of the heat collected, heat loss, temperature rise of water and heat-collecting efficiency with the velocity of ambient air. As the velocity of ambient air rises from 0 m/s to 4 m/s the heat loss increases by about 0.5 W. While collector efficiency reduces slightly by about 1% and outlet temperature of water decreases by 2 K. As velocity of ambient air increase, convective heat transfer coefficients of glass cover are raised and hence heat losses through the glass cover is enhanced. This brings little effects on collector efficiency because main heat resistance exists in the air layer. The separation of CPC weakens the convection intensity in air layer, reducing the influence of convective heat transfer coefficients on collector efficiency. Temperature distribution on outlet profile of the computational domain (see Fig. 16) also indicates that velocity of ambient air affects the temperature gradient from air layer to glass cover. However, the higher the velocity of ambient air, the smaller the impacts are.

4.5. Effect of glass thickness

Simulation are performed for the glass thickness of 2, 3, 4, 5 and 6 mm, respectively. The corresponding glass transmittances for these thicknesses are given in Table 6. The transmittance decreases slightly with increasing thickness. The solar irradiation through the glass cover and the collected heat of the collector decreases slightly. Figure 18 shows the variations of the heat collected, heat loss, temperature rise of water and heat-collecting efficiency with the glass thickness. As the thickness increases, both the heat collected and the temperature rise of water increase slightly and then decrease slightly. The heat loss and efficiency appear almost the same with increasing thickness. In

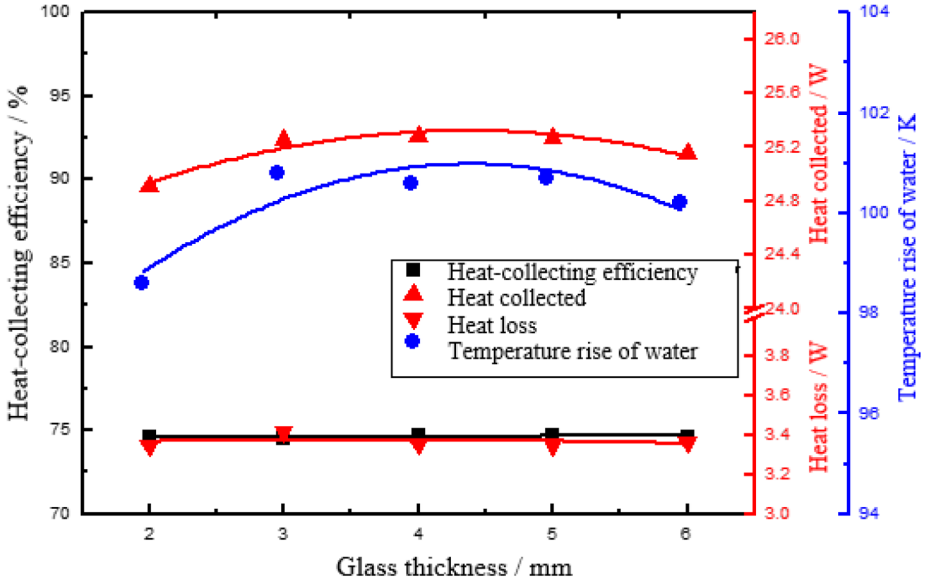

Fig. 18. Effect of glass thickness on the thermal performance of the CPC-CSC.

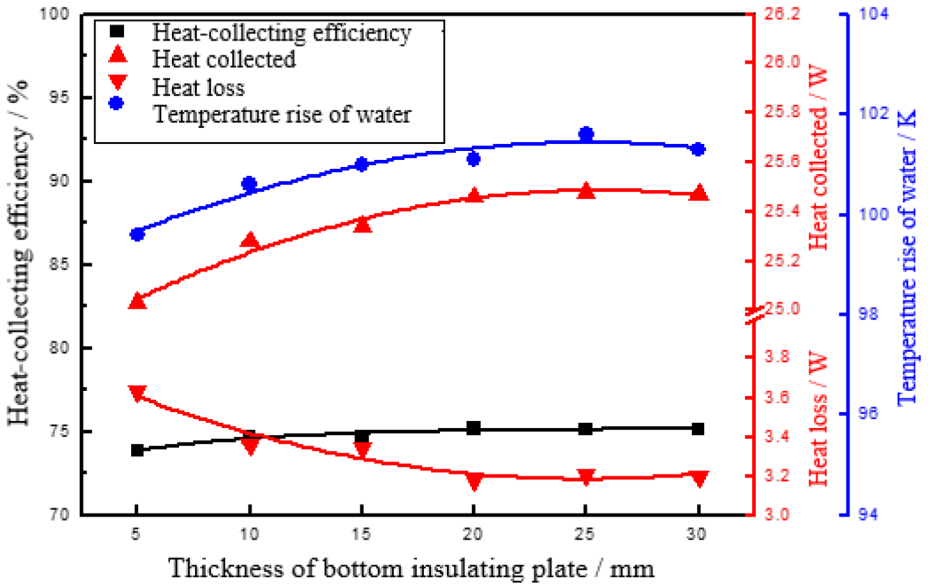

Fig. 19. Effect of insulation thickness on the thermal performance of the CPC-CSC.

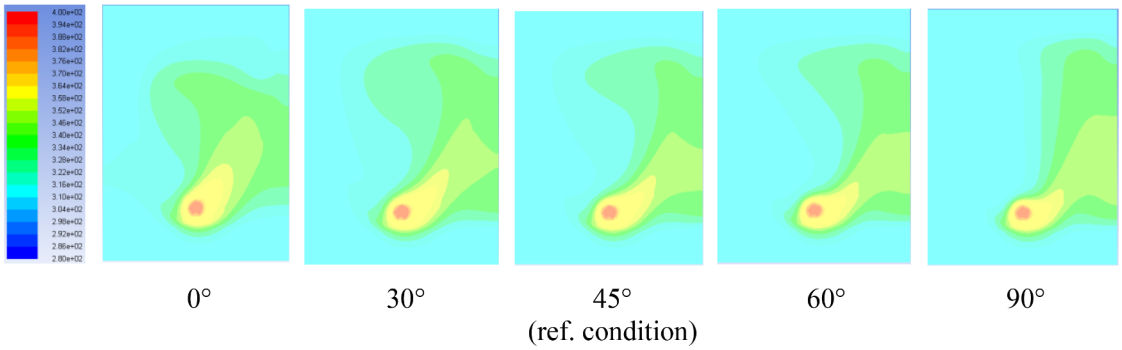

Fig. 20. Temperature profiles at the outlet plane for different inclination angles.

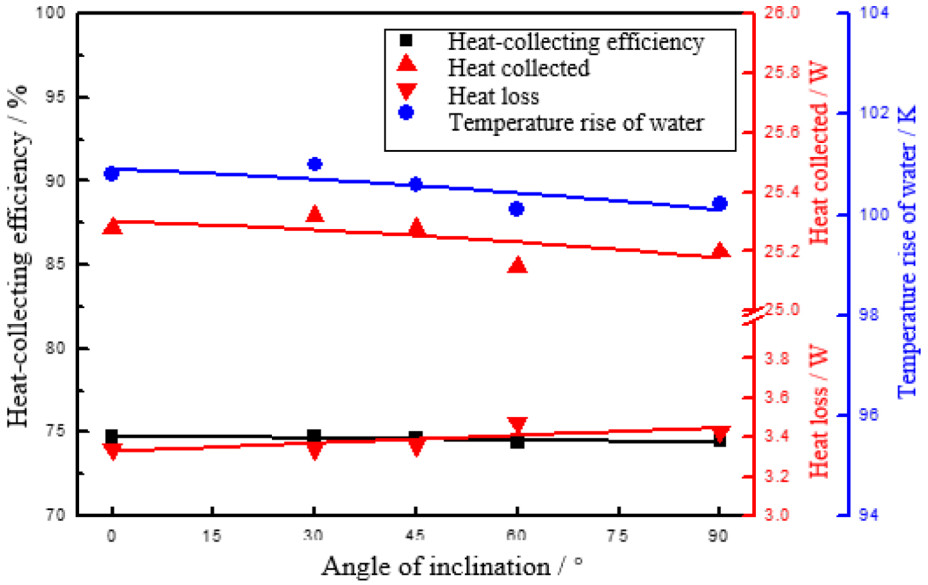

Fig. 21. Effect of inclination angles on the thermal performance of the CPC-CSC.

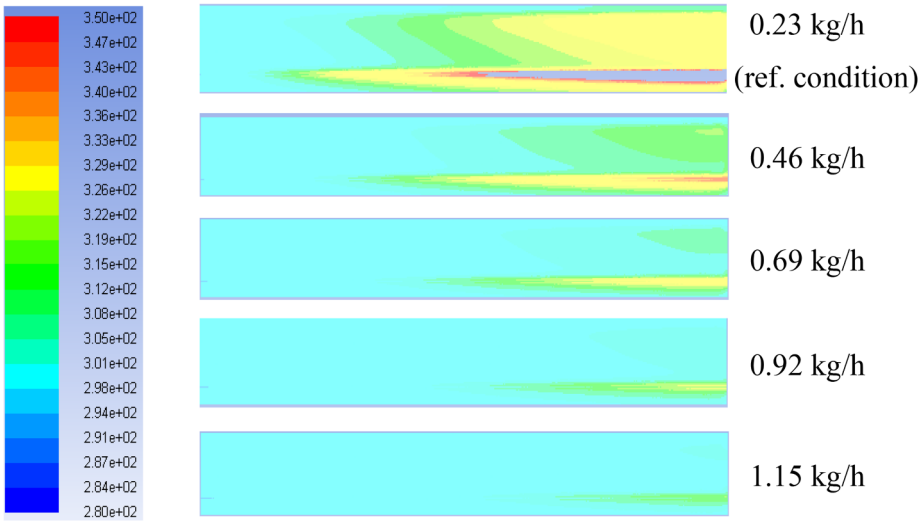

Fig. 22. Temperature profiles at the plane × = 0 for different mass flow rates.

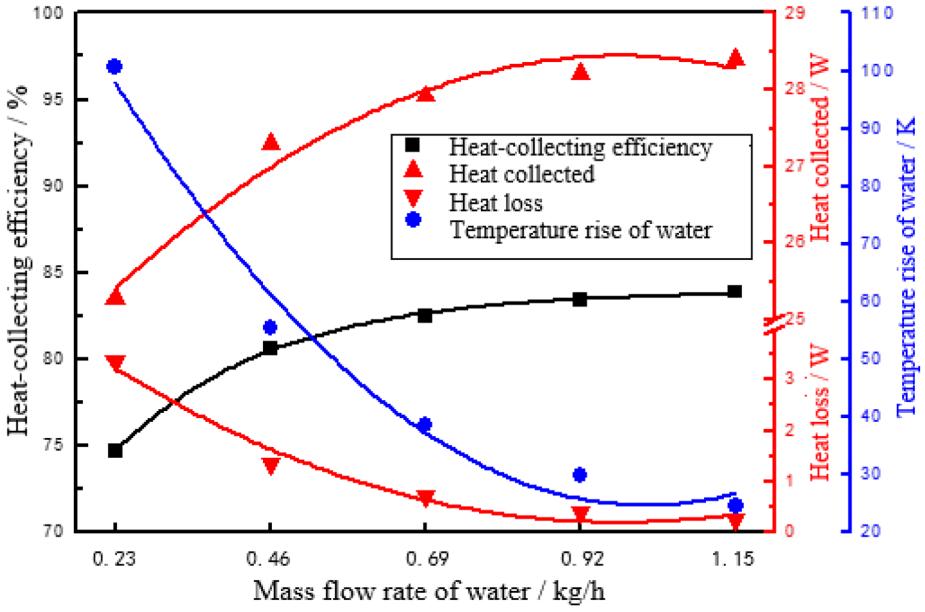

Fig. 23. Effect of mass flow rate on the thermal performance of the CPC-CSC.

practice, a thickness of 4 mm can meet the requirements for structural safety performance.

4.6. Effect of insulation thickness

Part of heat inside the collector is lost through insulation baseplate. Simulations are performed for the baseplate insulation thickness from 5 to 30 mm, respectively. Fig. 19 shows the variations of the heat collected, heat loss, temperature rise of water and heat-collecting efficiency with the thickness of baseplate insulation. It suggests that with increasing insulation thickness, the heat loss through insulation baseplate decreases by less than 0.5 W, the heat collected increases by less than 0.5 W, the temperature rise of water increases by about 2 K and the collector efficiency increase slightly. That is, the thickness of insulation baseplate has little influence on the heat losses of the computational domain.

4.7. Effect of inclination angle

The inclination angle is defined as the angle between the collector and horizontal. Various inclination angles can affect collector efficiency and heat losses mainly by the impact on convection in air layer. Simulations are performed for five inclination angles from 0° to 90°. Fig. 20 shows the temperature profile at the plane for five inclination angles. When inclination angle increases, heat distribution on outlet surface changes merely. Temperature distribution on x-direction profile shows that the increase of inclination angle can lead to the rise of air temperature above and below the copper collector tube near the outlet, indicating higher heat losses at these parts.

Figure 21 shows the variations of the heat collected, heat loss, temperature rise of water and heat-collecting efficiency with the inclination angle. It introduces that as the inclination angle increase, the heat losses increase slightly. The heat collected, the temperature rise of water and efficiency decrease slightly with increasing inclination angle. It is noted that in the actual experiment, solar radiation absorbed by the collector varies intensely at diverse inclination angles. When inclination angle is 90°, solar irradiation absorbed by the collector is smaller, laying great impacts on heat collection and collector efficiency. So, the collected heat of the solar energy should be fully considered in the actual installation process of collectors.

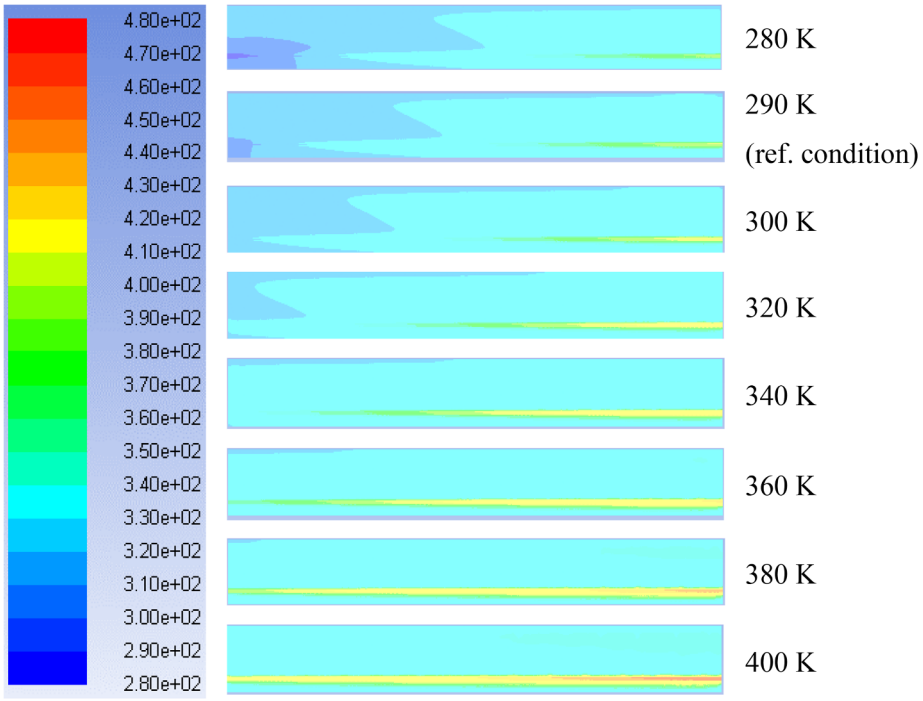

Fig. 24. Temperature profiles at plane × = *0* for different inlet temperatures of water.

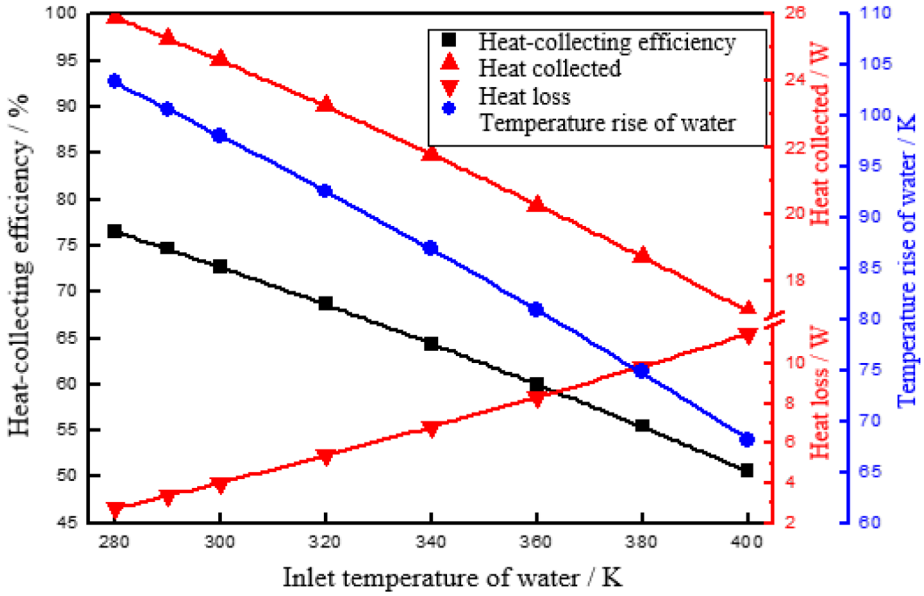

Fig. 25. Effect of inlet temperature of water on thermal performance of CPC-CSC.

4.8. Effect of mass flow rate of water

Simulations are performed for five mass flow rate of wate ranging from 0.23 kg/h to 1.15 kg/h. Fig. 22 shows the temperature profiles at the plane $x = 0$ for the five mass flow rates. Fig. 23 shows the variations of the heat collected, heat loss, temperature rise of water and heat-collecting efficiency with the mass flow rate of water. The temperature rise of water between the inlet and outlet can reach 100 K. These temperatures fall quickly as the mass flow rate increases from 0.23 kg/h to 0.92 kg/h and fall slightly as the mass flow rate further increases from 0.92 kg/h to 1.15 kg/h. It is seen from Fig. 23 that as the mass flow rate increases from 0.23 kg/h to 0.92 kg/h, the heat loss decreases from about 3.5 W to 0.5 W, the heat collected increases from about 25.5 W to 28.0 W, the temperature rise of water decreases from 100 K to 30 K and the efficiency increases from 75% to 83%. Further increasing the mass flow rate, the heat loss, heat collected, temperature rise of water and collector efficiency vary slightly. When the mass flow rate is 1.15 kg/h, the maximum collector efficiency can achieve 83.8%. The results suggest that the new collector can match a wide range of collecting temperature with a higher collector efficiency in low-to-medium temperatures.

4.9. Effect of inlet temperature of water

Simulations are performed for eight inlet temperature of water ranging from 280 K to 400 K. Fig. 24 shows the temperature profiles at the plane $x = 0$ for different inlet temperatures of water. Fig. 25 shows the variations of the heat collected, heat loss, temperature rise of water

and heat-collecting efficiency with the inlet temperature of water. The raises of outlet temperatures of water correspond to the increases of inlet temperatures of water and also the air temperature in the air layer. Air convection is enhanced, together with heat losses through glass cover and insulation baseplate. Therefore, collector efficiency drops obviously. As the inlet temperature of water increases from 280 K to 400 K, the heat loss almost linearly increases from about 2.5 W to 11.0 W and the heat collected, the temperature rise of water and efficiency almost linearly decrease from 26 W to 17.5 W, 103 K to 67 K and 74.7% to 50.6%, respectively. Compared with flat-plate collector, the new solar collector can obtain higher heat-collecting temperature with relatively high collector efficiency, meeting the requirements for the medium-temperature solar collector.

5. Conclusions

A novel compound parabolic concentrator-capillary tube solar collector (CPC-CSC) has been developed. It has a concentration ratio of 4.22 and the same thickness of flat-plate solar collectors. The new solar collector has been modeled and numerically simulated in wide ranges of working conditions. Experiments have been conducted to examine its operating characteristics and thermal performance. The effects of the solar irradiation intensity, mass flow rate and inlet temperature of water, velocity of ambient air, glass thickness, insulation thickness and inclination angle on the thermal performance have been investigated. The following conclusions may be drawn.

1) When the solar irradiation intensity is 1000 W/m^2 and inlet water temperature is 290 K, the measured transient efficiency of the new collector is 66.0%, while the efficiency calculated by the numerical simulation is 74.7%. This difference may be attributed to the neglect of the heat loss from the side surfaces in the simulation;
2) The heat loss by convective heat transfer through air layer is found to be the main heat loss. The CPCs can separate the air layer into small cells, reduce convection and heat leakage and thus improve the collector efficiency. The rise in surface temperature of the collector tubes enhances the convective heat transfer in the air layer and thus the collector efficiency is relatively lower for higher surface temperature of the collector tubes;
3) As the solar irradiation intensity increases, the surface temperature of the collector tubes rises and hence the convection in the air layer is enhanced, leading to decrease in collector efficiency. When the solar irradiation intensity is 300 W/m^2, solar collector efficiency is 79.8%. While a collector efficiency of 74.7% corresponds to solar irradiation intensity of 1000 W/m^2. The velocity of ambient air, glass thickness, insulation thickness, and inclination angle affect little on the performance of the solar collector;
4) As the mass flow rate varies from 0.23 kg/h to 1.15 kg/h, the heat losses through the glass cover and insulation baseplate decrease, and collector efficiency increases. When mass flow rate is 1.15 kg/h, the maximum collector efficiency can achieve 83.8%. The new collector can match a wide range of collecting temperature with higher efficiency in low-to-medium temperatures.
5) As the inlet temperature of water rises from 290 K to 400 K, the collector efficiency drops from 74.7% to 50.6%. When the inlet temperature of water is 400 K, the outlet temperature of water reaches 467 K and the efficiency fall to 50.6%. Compared with the flat-plate solar collector, the solar collector in the present work can obtain higher heat-collecting temperature with relatively high efficiency, meeting the requirements for the medium-temperature solar collectors.

Declaration of Competing Interest

The authors declare that they have no known competing financial interests or personal relationships that could have appeared to influence the work reported in this paper.

Acknowledgments

The work was funded by the National Natural Science Foundation of China (51506004), Beijing Natural Science Foundation (3162009), Scientific Research Project of Beijing Municipal Education Commission (KM201410016001), Beijing Youth Top-notch Talent Support Program and Fundamental Research Fund for Beijing University of Civil Engineering and Architecture (X18101).

References

[1] Shafieian A, Khiadani M, Nosrati A. Strategies to improve the thermal performance of heat pipe solar collectors in solar systems: a review. Energy Convers Manage 2019;183:307–31.
[2] Raj P, Subudhi S. A review of studies using nanofluids in flat-plate and direct absorption solar collectors. Renew Sustain Energy Rev 2018;84:54–74.
[3] Zhu T, Diao Y, Zhao Y, et al. Experimental study on the thermal performance and pressure drop of a solar air collector based on flat micro-heat pipe arrays. Energy Convers Manage 2015;94:447–57.
[4] Kundu B. Analytic method for thermal performance and optimization of an absorber plate fin having variable thermal conductivity and overall loss coefficient. Appl Energy 2010;87(7):2243–55.
[5] Rui Duan. The efficiency of new solar flat-plate collector. Adv Mater Res 2011;347–353:1337–41.
[6] Bhowmik H, Amin R. Efficiency improvement of flat plate solar collector using reflector. Energy Rep 2017;3:119–23.
[7] Beikircher T, Möckl M, Osgyan P, et al. Advanced solar flat plate collectors with full area absorber, front side film and rear side vacuum super insulation. Sol Energy Mater Sol Cells 2015;141:398–406.
[8] He QB, Zeng SQ, Wang SF. Experimental investigation on efficiency of flat-plate solar collectors with Cu-H2O nanofluids. Acta Energiae Solaris Sinica 2015;88:165–71.
[9] Ahmadi A, Ganji DD, Jafarkazemi F. Analysis of utilizing Graphene nanoplatelets to enhance thermal performance of flat plate solar collectors. Energy Convers Manage 2016;126:1–11.
[10] Tian M, Su Y, Zheng H, et al. A review on the recent research progress in the compound parabolic concentrator (CPC) for solar energy applications. Renew Sustain Energy Rev 2018;82:1272–96.
[11] Pranesh V, Velraj R, Christopher S, et al. A 50 year review of basic and applied research in compound parabolic concentrating solar thermal collector for domestic and industrial applications. Sol Energy 2019;187:293–340.
[12] Li X, Dai YJ, Li Y, et al. Comparative study on two novel intermediate temperature CPC solar collectors with the U-shape evacuated tubular absorber. Sol Energy 2013;93:220–34.
[13] Zheng WD, Yang L, Zhang H, et al. Numerical and experimental investigation on a new type of compound parabolic concentrator solar collector. Energy Convers Manage 2016;129:11–22.
[14] Xu RJ, Zhang XH, Wang RX, et al. Experimental investigation of a solar collector integrated with a pulsating heat pipe and a compound parabolic concentrator. Energy Convers Manage 2017;148:68–77.
[15] Gu X, Taylor RA, Morrison G, et al. Theoretical analysis of a novel, portable, CPC-based solar thermal collector for methanol reforming. Appl Energy 2014;119(15):467–75.
[16] Pradhan D, Mitra D, Neogi S. Thermal Performance of a Heat Pipe Embedded Evacuated Tube Collector in a Compound Parabolic Concentrator. Energy Procedia 2016;90:217–26.
[17] Al-Imam MFI, Beg RA, Rahman MS, et al. Performance of PVT solar collector with compound parabolic concentrator and phase change materials. Energy Build 2016;113:139–44.
[18] Khalifa AJN, Al-Mutawalli SS. Effect of two-axis sun tracking on the performance of compound parabolic concentrators. Energy Convers Manage 1998;39(10):1073–9.
[19] Zou B, Dong J, Yao Y, et al. An experimental investigation on a small-sized parabolic trough solar collector for water heating in cold areas. Appl Energy 2016;163:396–407.
[20] Chamsa-Ard W, Sukchai S, Sonsaree S, et al. Thermal performance testing of heat pipe evacuated tube with compound parabolic concentrating solar collector by ISO 9806–1. Energy Procedia 2014;56:237–46.
[21] Oommen R, Jayaraman S. Development and performance analysis of compound parabolic solar concentrators with reduced gap losses-oversized reflector. Energy Convers Manage 2001;42(11):1379–99.
[22] Réné Tchinda. Thermal behaviour of solar air heater with compound parabolic concentrator. Energy Convers Manage 2008;49(4):529–40.
[23] Abdullahi B, Al-Dadah RK, Mahmoud S, et al. Optical and thermal performance of double receiver compound parabolic concentrator. Appl Energy 2015;159:1–10.
[24] Chaves J. Introduction to nonimaging optics. CRC Press; 2017.
[25] Wang Y, Zhu Y, Chen H, et al. Performance analysis of a novel sun-tracking CPC heat pipe evacuated tubular collector. Appl Therm Eng 2015;87:381–8.
[26] Zhang D, Tao H, Wang M, et al. Numerical simulation investigation on thermal performance of heat pipe flat-plate solar collector. Appl Therm Eng 2017;118:113–26.
[27] Santos-González I, García-Valladares O, Ortega N, et al. Numerical modeling and experimental analysis of the thermal performance of a compound parabolic concentrator. Appl Therm Eng 2016;114:1152–60.
[28] Liu L, Jia Y, Lin Y, et al. Numerical study of a novel miniature compound parabolic concentrating photovoltaic/thermal collector with microencapsulated phase change slurry. Energy Convers Manage 2017;153:106–14.